Inorganic Chemistry

Article

pubs.acs.org/IC

Iron(III) Complexes of a Pyridoxal Schiff Base for Enhanced Cellular Uptake with Selectivity and Remarkable Photocytotoxicity

Uttara Basu,[†] Ila Pant,[‡] Akhtar Hussain,[†] Paturu Kondaiah,*[,‡] and Akhil R. Chakravarty*[,†]

[†]Department of Inorganic and Physical Chemistry and [‡]Department of Molecular Reproduction, Development and Genetics, Indian Institute of Science, Bangalore 560012, Karnataka, India

Supporting Information

ABSTRACT: Iron(III) complexes of pyridoxal (vitamin B6, VB6) or salicylaldehyde Schiff bases and modified dipicolylamines, namely, $[Fe(B)(L)](NO_3)$ (**1**−**5**), where B is phenyl-*N*,*N*-bis((pyridin-2-yl)methyl)methanamine (phbpa in **1**), (anthracen-9-yl)-*N*,*N*-bis((pyridin-2-yl)methyl)methanamine (anbpa in **2**, **4**) and (pyren-1-yl)-*N*,*N*-bis((pyridin-2-yl)-methyl)methanamine (pybpa in **3**, **5**) (H_2L^1 is 3-hydroxy-5-(hydroxymethyl)-4-(((2-hydroxyphenyl)imino)methyl)-2-methylpyridine (**1**−**3**) and H_2L^2 is 2-[(2-hydroxyphenyl-imino)methyl]phenol), were prepared and their uptake in cancer cells and photocytotoxicity were studied. Complexes **4** and **5**, having a non-pyridoxal Schiff base, were prepared to probe the role of the pyridoxal group in tumor targeting and cellular uptake. The PF_6 salt (**1a**) of complex **1** is structurally characterized. The complexes have a distorted six-coordinate FeN_4O_2 core where the metal is in the +3 oxidation state with five unpaired electrons. The complexes display a ligand to metal charge transfer band near 520 and 420 nm from phenolate to the iron(III) center. The photophysical properties of the complexes are explained from the time dependent density functional theory calculations. The redox active complexes show a quasi-reversible Fe(III)/Fe(II) response near −0.3 V vs saturated calomel electrode. Complexes **2** and **3** exhibit remarkable photocytotoxicity in various cancer cells with IC_{50} values ranging from 0.4 to 5 μM with 10-fold lower dark toxicity. The cell death proceeded by the apoptotic pathway due to generation of reactive oxygen species upon light exposure. The nonvitamin complexes **4** and **5** display 3-fold lower photocytotoxicity compared to their VB6 analogues, possibly due to preferential and faster uptake of the vitamin complexes in the cancer cells. Complexes **2** and **3** show significant uptake in the endoplasmic reticulum, while complexes **4** and **5** are distributed throughout the cells without any specific localization pattern.

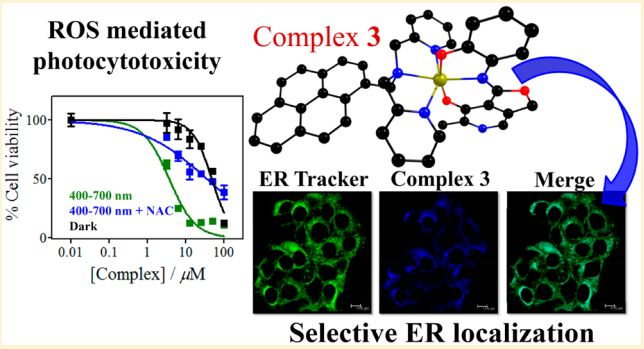

INTRODUCTION

A novel strategy to design and develop new generation of chemotherapeutic or photo-chemotherapeutic agents is to direct them to other cellular organelles instead of the nucleus in order to circumvent the drawbacks associated with nuclear DNA targeting anticancer drugs.[1−5] The resistance of cisplatin or its analogues can be partially explained by the extensive repair of the cisplatin-DNA and related adducts by the nucleotide excision repair (NER) pathway which reduces the efficacy of the drug.[6,7] Gasser et al. have explored the biological effects of ruthenium complexes of 2-pyridyl-2-pyrimidine-4-carboxylic acid showing excellent anti-proliferative property in various cell lines with predominant localization in the mitochondria, disrupting the mitochondrial membrane potential in HeLa cells.[8] Neamati and co-workers have reported a selective mitochondria targeting chlorambucil with remarkable cytotoxicity in breast and pancreatic cancer cells.[9] Dhar et al. recently reported a mitochondria targeting cisplatin analogue, namely, Platin-M that disrupts the mitochondrial genome instead of its conventional target, the nuclear DNA.[10,11] The FDA approved drug Photofrin, used in photodynamic therapy (PDT) of cancer, is also known for its therapeutic action in red light of 633 nm involving disruption of the mitochondria.[12−17] Sadler et al. discussed the disruption of mitochondrial function as an attractive target for anticancer drug design in a recent article.[18]

While targeting mitochondria provides a novel pathway for apoptotic cell death, another equally useful strategy could be to target the endoplasmic reticulum (ER) and induce stress in the ER of the cells which is associated with protein folding.[19−21] The ER stress which can occur as a consequence of exogenous or endogenous effects of an anticancer agent could disrupt the folding capacity of the ER. Severe or prolonged stress could result in toxic signals that cause intrinsic apoptosis through ER stress response (ERSR).[22,23] Cytotoxicity arising from ERSR involving the reactive oxygen species (ROS) formed on photoactivation of the photosensitizer at specific sites of cancer cells inducing tumor damage is a novel way to target cancer cells. Development of such tumor specific delivery agents to the

Received: November 17, 2014

DOI: 10.1021/ic5027625
Inorg. Chem. XXXX, XXX, XXX−XXX

ER could improve the efficacy of an anticancer agent by distinguishing normal cells from the tumor cells. PDT which has evolved as a minimally invasive treatment procedure for cancer relies on the production of ROS upon photoactivation of a photosensitizer (PS).[24−26] The PS on activation with light of suitable wavelength goes to its singlet excited state from where it may reach a low lying triplet excited state by intersystem crossing (ISC). This is followed by the energy transfer to molecular oxygen to form singlet oxygen ($^1O_2$) via type-II process. The alternate pathway is an electron transfer reaction to produce hydroxyl ($HO^•$) and/or superoxide ($O_2^{•−}$) radicals which is called the photoredox pathway. These cytotoxic ROS are responsible for cell death. Thus, the delivery vehicle should consist of a tumor targeting group appended to ROS generator for the desired localized photocytotoxicity.

We have recently reported ternary iron(III) complexes having photosensitizing moieties showing significant photocytotoxicity in red light.[27] These complexes, however, show significant nuclear localization and target the nuclear DNA for their cytotoxic activity. With an objective to target other cellular organelle, we have chosen vitamin B6 (VB6) in our ligand design to prepare new iron(III) complexes with the knowledge of ER targeted photocytotoxicity by an oxovanadium(IV) complex of VB6.[28] VB6 is a biologically important molecule which plays a major role in various metabolic, physiological, and developmental processes.[29,30] It is an important cofactor in various cellular processes like DNA biosynthesis for cell growth and proliferation. Besides, VB6 plays important role as a protective factor in various cancers, and VB6 derivatives decrease cell proliferation and angiogenesis and it is implicated in reducing tumorigenesis.[31] Though the molecular mechanism of VB6 remains elusive, it is known that most of VB6 is transported to the liver and taken up by facilitated diffusion through specific VB6 transporting membrane carriers (VTC) into the cells.[32−35] Serine hydroxymethyltransferase (SHMT) is an enzyme with a profound role in DNA biosynthesis which depends on VB6. The activity of this enzyme increases during DNA duplication in the proliferating tumor cells as a result of which the consumption of VB6 is also increased. Thus, to meet the increased VB6 requirement in the cancer cells, it is absorbed from the neighboring cells. Since tumor cells have a higher demand for VB6, the VB6 conjugated molecules can accomplish improved entry into tumor cells. As VB6 or its conjugates are known to show higher cellular uptake inside the cancer cells, the iron(III) complex of the Schiff base ligand derived of this molecule is likely to increase the cellular uptake and selectivity of the complex.[36]

Combining the aforementioned strategies, we have synthesized new ternary iron(III) complexes, namely, [Fe(B)(L)]-(NO_3) (**1**−**5**) of dipicolylamine bases (B: phbpa, anbpa, pybpa) and tridentate Schiff base ligands (H_2L) derived from pyridoxal (VB6, H_2L^1 in complexes **1**−**3**) or salicylaldehyde (H_2L^2 in **4**, **5**) (Chart 1). The pyridoxal moiety is anticipated to facilitate the diffusion of the complexes inside the cells ensuring faster cellular uptake and hence better cytotoxicity. To substantiate our hypothesis, control complexes **4** and **5** having a Schiff base ligand of salicylaldehyde are prepared, and their various biological properties are studied and compared. The Schiff base ligands having phenolic groups are envisaged to bind strongly to iron(III) to furnish an intense charge transfer (CT) band in visible light which is used for inducing photocytotoxicity. The tridentate ligands are also expected to stabilize iron in its +3 oxidation state and to avoid any possible leaching

Chart 1. Schematic Representation of the Ternary Iron(III) Complexes 1−5

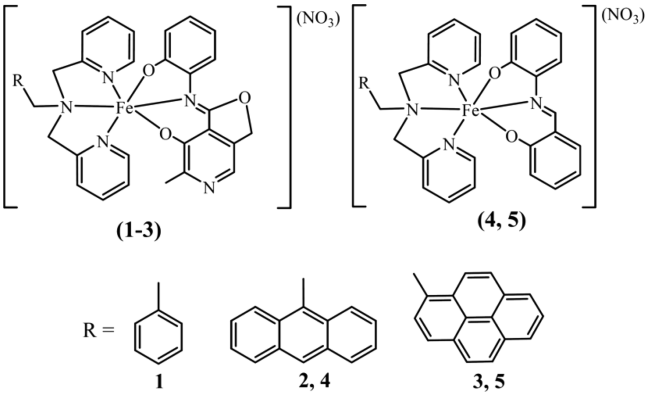

of the metal from the complex in a biological medium. The *N*,*N*,*N*-donor tridentate dipicolylamine base is functionalized with pendant aromatic groups like phenyl (**1**), anthracenyl (**2**, **4**) and pyrenyl (**3**, **5**) for better photocytotoxic activity. Complex **1** without a photoactive group is used as a control. The anthracenyl and pyrenyl groups as fluorescent tags are used to trace the molecule inside the cells from an imaging study. The photocytotoxicity of the complexes, their differential uptake properties inside the cells, and their cellular localization are investigated. The notable results of this work include remarkable photocytotoxicity in visible light (400−700 nm) of the VB6 derived complexes and apoptotic cell death via generation of ROS in cancer cells by predominantly affecting the ER as compared to the nonvitamin complexes.

EXPERIMENTAL SECTION

Materials and Methods. The chemicals were procured from various commercial sources (s.d. Fine Chemicals, India; Sigma-Aldrich, U.S.A.) and used without further purification. The solvents were dried or distilled using standard procedures.[37] 2′,7′-Dichlorofluorescein diacetate (DCFDA), 3-(4,5-dimethylthiazol-2-yl)-2,5-diphenyltetrazolium bromide (MTT), propidium iodide (PI), Dulbecco's modified eagle medium (DMEM), Dulbecco's phosphate buffered saline (DPBS), Annexin-V/PI kit and fetal bovine serum (FBS) were obtained from Sigma (U.S.A.). ER tracker green was procured from Invitrogen U.S.A.

The elemental analysis was conducted with a Thermo Finnigan Flash EA 1112 CHNS analyzer. The infrared and electronic spectra were obtained using Bruker Alpha and PerkinElmer Spectrum 650 spectrophotometers, respectively. Emission spectra were recorded using a PerkinElmer LS 55 spectrophotometer. Molar conductivities of the complexes were measured with a Control Dynamics (India) conductivity meter. Electrochemical studies were performed using EG&G PAR model 253 VersaStat potentiostat/galvanostat with electrochemical analysis software 270 and a three electrode setup. A glassy carbon electrode was used as the working electrode, a platinum wire was used as an auxiliary electrode, and a saturated calomel electrode (SCE) served the purpose of a reference electrode. Tetrabutylammonium perchlorate (TBAP, 0.1 M), used as a supporting electrolyte, was prepared from dropwise addition of perchloric acid ($HClO_4$) to tetrabutylammonium bromide in water with vigorous stirring followed by filtration of the white solid and thorough washing with water to remove the acid. Care has to be taken during production and handling of TBAP as contact with combustible material may cause fire. It should not be heated (Caution!). Electrospray ionization mass spectrometry (ESI-MS) data were obtained using an Agilent 6538 Ultra high definition (UHD) accurate Mass-Q-TOF (LC-HRMS) instrument. ^1H NMR spectral measurements were done with a Bruker 400 MHz NMR spectrometer.

DOI: 10.1021/ic5027625
Inorg. Chem. XXXX, XXX, XXX−XXX

Fluorescence assorted cell sorting experiments were done using FACS Verse instrument (BD Biosciences). Magnetic susceptibility measurements of the complexes at 300 K were done with solid samples using MPMS SQUID VSM (Quantum Design, USA). Confocal microscopy images were acquired using Leica microscope (TCS, SP5) with oil immersion lens having magnification of 63×.

Synthesis of the Ligands. The dipicolylamine derivatives were synthesized following reported procedures.[38] The Schiff base ligands were synthesized by refluxing an ethanol solution of pyridoxal hydrochloride (neutralized with 1 equiv of triethylamine) or salicylaldehyde and 2-aminophenol for 1−3 h (Scheme S1, Supporting Information). To prepare the VB6 Schiff base (H_2L^1), pyridoxal hydrochloride (0.21 g, 1 mmol) was dissolved in dry ethanol (10 mL) and was neutralized with triethylamine (0.10 g, 1 mmol). 2-Aminophenol (0.11 g, 1 mmol) also dissolved in dry ethanol (5 mL) was added to the reaction mixture and was refluxed for 3 h. The orange precipitate was filtered, washed thoroughly with ether, and crystallized from ethanol to give yellow orange crystals (yield: ∼90%). The other Schiff base (H_2L^2) was prepared by reacting salicylaldehyde (0.12 g, 1 mmol) in dry ethanol (5 mL) with 2-aminophenol (0.11 g, 1 mmol) also in dry ethanol (5 mL) on stirring at room temperature for 1 h. The orange precipitate was filtered and washed with ether. It was crystallized from ethanol to give bright orange crystals (yield: ∼95%). Characterization data for H_2L^1: ^{1}H NMR (DMSO-d_6, 400 MHz) δ (ppm): 14.702 (s, 1H), 10.011 (s, 1H), 9.234 (s, 1H), 7.953 (s, 1H), 7.480 (m, 1H), 7.482−7.458 (m, 1H), 7.224−7.182 (m, 1H), 7.022−6.999 (m, 1H), 6.946−6.905 (m, 1H) 5.408 (t, J = 5.2, 1H), 4.764 (d, J = 5.6, 2H), 2.542 (s, 3H) (s, singlet; t, triplet; m, multiplet; J, coupling constant). ESI-MS (m/z): 259.1082 $[M + H]^+$. Characterization data for H_2L^2: ^{1}H NMR (DMSO-d_6, 400 MHz) δ (ppm): 13.787 (s, 1H), 9.747 (s, 1H), 8.959 (s, 1H), 7.619−7.596 (m, 1H), 7.404−7.343 (m, 2H), 7.146−7.104 (m, 1H), 6.966−6.857 (m, 4H), 3.374 (s, 3H).

Synthesis of [Fe(phbpa/anbpa/pybpa)(L^1/L^2)](NO_3) (1−5). The complexes were synthesized by a general procedure in which $Fe(NO_3)_3{\cdot}9H_2O$ (0.41 g, 1 mmol) was dissolved in methanol (5 mL) to which was added the dipicolylamine base [phbpa for **1**, anbpa for **2** and **4**, and pybpa for **3** and **5**, 1 mmol] also dissolved in methanol (5−10 mL) (Scheme S2, Supporting Information). The reaction mixture was stirred for 1 h. The Schiff base ligand H_2L^1 (for **1**−**3**, 0.26 g, 1 mmol) or H_2L^2 (for **4** and **5**, 0.21 g, 1 mmol) was dissolved in methanol (6 mL) and treated with 2 equiv of triethylamine (0.20 g, 2 mmol). The solution having a dianionic Schiff base was added to the reaction mixture and stirred at room temperature for 3 h. The brown precipitate was isolated by filtration followed by thorough washing with diethyl ether and drying in a vacuum over P_4O_{10}.

*[Fe(phbpa)(L^1)](NO_3) (**1**).* Yield, ∼75% (0.49 g). Anal. Calcd for $C_{33}H_{29}FeN_6O_6$ (Mw: 661.46): C, 59.92; H, 4.42; N, 12.71. Found: C, 59.81; H, 4.31; N 12.63. ESI-MS in MeOH (m/z): 599.1650 $[M-NO_3]^+$. Molar conductance in DMF (Λ_M): 74 S m^2 M^{-1}. FT-IR: 3054 w, 1575 m, 1460 s, 1420 s, 1380 s, 1290 vs, 1254 vs, 1146 s, 1043 m, 1005 s, 872 w, 820 m, 740 s, 576 m, 524 m (vs, very strong; s, strong; m, medium; w, weak). UV−visible in DMF [λ_{max}/nm (ε/M^{-1} cm^{-1})]: 576 (4420), 420 (19080). μ_{eff} (298 K) = 5.84 μ_B.

*[Fe(anbpa)(L^1)](NO_3) (**2**).* Yield, ∼70% (0.54 g). Anal. Calcd for $C_{41}H_{33}FeN_6O_6$ (Mw: 761.58): C, 64.66; H, 4.37; N, 11.03. Found: C, 64.79; H, 4.46; N 11.21. ESI-MS in MeOH (m/z): 699.2209 $[M-NO_3]^+$. Molar conductance in DMF (Λ_M): 71 S m^2 M^{-1}. FT-IR: 3052 w, 1578 m, 1440 m, 1390 s, 1290 vs, 1160 m, 1020 m, 850 w, 820 m, 742 s, 650 w, 547 w, 472 w. UV−visible in DMF [λ_{max}/nm (ε/M^{-1} cm^{-1})]: 517 (2520, sh), 413 (8960, sh), 389 (16460), 370 (16700), 350 (13950), 335 (11080) (sh, shoulder). μ_{eff} (298 K) = 5.80 μ_B.

*[Fe(pybpa)(L^1)](NO_3) (**3**).* Yield, ∼70% (0.56 g). Anal. Calcd for $C_{41}H_{33}FeN_6O_6$ (Mw: 785.60): C, 65.74; H, 4.23; N, 10.70. Found: C, 65.59; H, 4.31; N 10.76. ESI-MS in MeOH (m/z): 723.2215 $[M-NO_3]^+$. Molar conductance in DMF (Λ_M): 77 S m^2 M^{-1}. FT-IR: 3052 w, 2352 w, 1600 s, 1385 s, 2490 w, 1590 w, 1295 vs, 1190 m, 1015 m, 840 m, 755 m, 552 w, 490 w. UV−visible in DMF [λ_{max}/nm (ε/M^{-1} cm^{-1})]: 519 (3060, sh), 403 (16450), 345 (48870), 330 (40960), 315 (25820), 300 (21220). μ_{eff} (298 K) = 5.80 μ_B.

*[Fe(anbpa)(L^2)](NO_3) (**4**).* Yield, ∼74% (0.53 g). Anal. Calcd for $C_{40}H_{32}FeN_5O_5$ (Mw: 718.56): C, 66.86; H, 4.49; N, 9.75. Found: C, 66.71; H, 4.41; N 9.83. ESI-MS in MeOH (m/z): 656.2350 $[M-NO_3]^+$. Molar conductance in DMF (Λ_M): 70 S m^2 M^{-1}. FT-IR: 3052 w, 2350 w, 1597 s, 1527 w, 1470 m, 1380 s, 1295 vs, 1145 w, 1020 m, 830 m, 745 s, 600 w, 530 w, 470 w. UV−visible in DMF [λ_{max}/nm (ε/M^{-1} cm^{-1})]: 501 (2140, sh), 408 (8710), 389 (10680), 369 (8280), 350 (8280). μ_{eff} (298 K) = 5.85 μ_B.

*[Fe(pybpa)(L^2)](NO_3) (**5**).* Yield, ∼71% (0.52 g). Anal. Calcd for $C_{42}H_{32}FeN_5O_5$ (Mw: 742.58): C, 67.93; H, 4.34; N, 9.43. Found: C, 67.78; H, 4.26; N 9.51. ESI-MS in MeOH (m/z): 680.1948 $[M-NO_3]^+$. Molar conductance in DMF (Λ_M): 73 S m^2 M^{-1}. FT-IR: 3052 w, 2350 w, 1597 s, 1530 w, 1470 m, 1380 s, 1295 vs, 1150 w, 1025 w, 845 s, 760 vs, 605 w, 540 w, 480 w. UV−visible in DMF [λ_{max}/nm (ε/M^{-1} cm^{-1})]: 507 (2760, sh), 415 (16590), 345 (33390), 330 (27790), 315 (21040), 300 (19240). μ_{eff} (298 K) = 5.81 μ_B.

X-ray Crystallographic Procedures. The crystal structure of complex **1** was obtained by single crystal X-ray diffraction method as its PF_6 salt (**1a**). The slow evaporation of a methanol−acetonitrile (3:2 v/v) solution of the complex resulted in the formation of dark red color crystals. Details of the crystallographic procedures are given as Supporting Information.[38] The CCDC deposition number is 1027849.

Theoretical Study. The geometries of the complexes **1**−**3** were optimized by density functional theory (DFT) using B3LYP level of theory and LanL2DZ basis set as implemented in Gaussian 09 program.[39,40] The initial coordinates were obtained from the crystal structure of **1a** which was used for the optimization of the structures of the complexes. The electronic transitions with their transition probability were obtained using linear response time dependent density functional theory (TDDFT).[41] The coordinates of the energy minimized structures and selected transitions in the visible region are listed in Tables S1 and S2 (Supporting Information).

Cellular Measurements. The photocytotoxicity of the complexes was studied using an MTT assay by following experimental procedures that have been reported earlier (see Supporting Information).[38] Cellular incorporation experiments were done to estimate the cellular uptake of the complexes **2**−**5** by flow cytometry in HeLa and HaCaT cells. Details of the experimental procedures are given in the Supporting Information.[38] The experiment was repeated with cells that were pretreated with pyridoxal hydrochloride (2 mM) 4 h prior to treatment with the complexes. Dose-dependent estimation of cellular uptake study was done to see the effect of varying concentrations of VB6 on the cellular uptake using flow cytometry. About 1 × 10^6 HeLa cells were plated per well of a six-well tissue culture plate in DMEM containing 10% FBS. After 24 h of incubation at 37 °C in a CO_2 incubator, varying concentrations of VB6 (2 mM, 1.5 mM, 1.0 mM, 0.5 mM, 0.25 mM, and 0.1 mM) were added and incubated in the dark for 4 h. It was followed by addition of complexes **3** or **5** (10 μM) and kept for another 4 h in the dark after which the supernatant was discarded by gently inverting the tube, and the cell pellet was suspended in 200 μL of DPBS. Flow cytometric analysis was performed using a FACS Verse machine (BD Biosciences) using the Pacific blue A filter. Cell cycle analysis was carried out to investigate the effect of complexes **1**−**5** on the progression of the cell cycle. HeLa or HaCaT cells were incubated with the complexes (10 μM) for 4 h followed by light irradiation (400−700 nm). Similarly, treated cells were also kept in the dark to serve as controls. Post irradiation cell processing was performed using standard procedures (see Supporting Information for details).[38] Annexin-V-FITC/PI assay experiment was performed to estimate the population of apoptotic cells by standard reported procedures (see Supporting Information).[38] A DCFDA assay was done to study the formation of ROS in HeLa or HaCaT cells treated with the photoactive complexes **2** or **3** under different conditions using 2′,7′-dichlorofluorescein diacetate (DCFDA). Post treatment processing of the cells was done following standard procedures (see Supporting Information).[38] The cellular localization pattern of the fluorescent complexes **2**−**5** (10 μM) inside HeLa and HaCaT cells was visualized using a confocal microscope (Leica, TCS, SP5). Standard experimental procedures were adopted for plating the

DOI: 10.1021/ic5027625
Inorg. Chem. XXXX, XXX, XXX−XXX

Table 1. Selected Physicochemical Data of the Complexes 1−5

complex	ESI-MS (m/z)[a]	IR[b]/cm^{-1}	λ/nm (ε/M^{-1} cm^{-1})[c]	λ_{em}[d]/nm (φ)	Λ_M[e]/S m^2 M^{-1}	E_f[f]/V (ΔE/mV)	μ_{eff}[g]
1	599.1650	1380	576 (4420, sh)		74	−0.26 (88)	5.84
2	699.2209	1390	517 (2520, sh)	423 (0.04)	71	−0.25 (86)	5.80
3	723.2215	1385	519 (3060, sh)	396 (0.06)	77	−0.26 (100)	5.80
4	656.2350	1380	501 (2140, sh)	426 (0.03)	70	−0.19 (90)	5.85
5	680.1948	1380	507 (2760, sh)	395 (0.05)	73	−0.20 (96)	5.81

[a]Molecular ion peak corresponding to $[M\text{-}NO_3]^+$ in MeOH. [b]Nitrate stretching in solid phase. [c]In DMF. sh, shoulder. [d]Emission of the complexes recorded in DMSO with the quantum yield values in parentheses with respect to anthracene and quinine sulfate. The fluorescence lifetimes are 9.89 × 10^{-9} s and 8.47 × 10^{-9} s for **2** and **3** respectively. The excitation wavelengths for **2**−**5** are 371, 346, 378, 341 nm, respectively. [e]Molar conductivity values in DMF at 25 °C. [f]Formal potential of the Fe(III)/Fe(II) redox couple vs SCE in DMF-0.1 M TBAP at a scan rate of 50 mV s^{-1}. [g]Effective magnetic moment of solid samples at 25 °C.

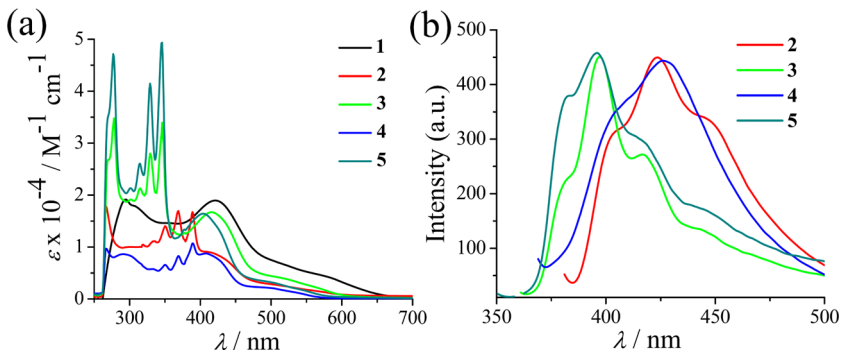

Figure 1. (a) UV−visible spectra of the complexes **1**−**5** in DMF in different color codes: black, **1**; red, **2**; green, **3**; blue, **4**; dark cyan, **5**. (b) Emission spectra of the complexes **2**−**5** in DMSO in color codes: red, **2**; dark cyan, **3**; blue, **4**; green, **5** [excitation wavelength (λ_{ex}) for **2**−**5** are 371, 346, 378, and 341 nm, respectively].

cells and processing them after treatment with the complexes (see Supporting Information).[38]

RESULTS AND DISCUSSION

Synthesis and General Aspects. The tridentate Schiff base (H_2L^1) of pyridoxal hydrochloride as yellow orange crystalline solid was prepared by reacting it with 2-aminophenol. A similar reaction of salicylaldehyde with 2-aminophenol gave the Schiff base H_2L^2 (Scheme S1, Supporting Information). The ligands were characterized from ^{1}H NMR in DMSO-d_6 and ESI-MS data (Figures S1−S4, Supporting Information). Ternary iron(III) complexes $[Fe(B)(L)](NO_3)$ (**1**−**5**) were prepared from a general reaction of $Fe(NO_3)_3.9H_2O$ with 1 equiv of the dipicolylamine derivative (B) and the Schiff base (H_2L^1/H_2L^2) in methanol in the presence of triethylamine (Chart 1, Scheme S2). The complexes were characterized from their physicochemical data (Table 1, Figures S5−S9, Supporting Information). Complex **1** having a pendant phenyl group on the dipicolylamine moiety was used as a control complex to explore the role of the anthracenyl and pyrenyl fluorophore moieties in showing the photocytotoxic effect. These groups enabled us to track the complexes inside the cells by cellular imaging. Complexes **4** and **5** having the salicylaldehyde Schiff base were also used as controls to ascertain the importance of the VB6 entity in complexes **1**−**3** in cellular uptake, localization, and photocytotoxicity.

The structure of the complexes was initially elucidated from the crystal structure of **1** as a PF_6 salt (**1a**) where the pyridoxal moiety was seen to undergo cyclization. The hydroxyl group forms a five-membered ring with the C=N moiety, which is discussed in a subsequent section. Such cyclization reactions are known to occur in the presence of protic or Lewis acids.[42−44] It appears that the cyclization occurs in the reaction mixture in the presence of Fe^{3+} which acts as a Lewis acid since the ligand alone did not show any trace of cyclized product. This is also corroborated from the ESI-MS data of the complexes **1**−**3** which show the molecular ion peak two units less than what would have been expected of a noncyclized Schiff base ligand (Figures S5−S9, Supporting Information). The IR spectra of the complexes **1**−**3** also suggest the absence of any free hydroxyl group (Figure S10, Supporting Information). The Schiff base ligands bear two phenolic groups which stabilize the metal in its +3 oxidation state and also generate an intense ligand to metal charge transfer (LMCT) band near 520 and 420 nm from phenolate π orbital to the dπ* orbital of iron (Figure 1a).[45,46] The LMCT bands enabled us to study the photocytotoxicity of the complexes in visible light. The anthracene and pyrene appended complexes **2**−**5** were emissive in the blue region near 400−420 nm upon excitation near 370 nm (Figure 1b). The quantum yield values were in the range of 0.03−0.05 with respect to pure anthracene and quinine sulfate as standards (Table 1). The complexes were 1:1 electrolytes in DMF giving molar conductivity values of ∼75 S m^2 M^{-1}. The complexes were redox active showing quasi-reversible Fe(III)−Fe(II) couple near −0.3 V in DMF-0.1 M TBAP (Figure S11, Supporting Information). The complexes gave magnetic moment values of ∼5.7 μ_B at 25 °C which is in accord with the high spin state of the iron(III) center.

X-ray Crystal Structure. Complex **1** was crystallized as a PF_6 salt (**1a**) and the crystals belonged to the triclinic space group $P\bar{1}$ with two molecules in the unit cell. Selected crystallographic parameters are given in Table 2. An ORTEP view of the molecule is shown in Figure 2 (Figure S12, Supporting Information, for unit cell packing diagram). Selected bond distances and angles are given in Table 3. The

DOI: 10.1021/ic5027625
Inorg. Chem. XXXX, XXX, XXX−XXX

Table 2. Selected Crystallographic Data for [Fe(phbpa)(L^1)](PF_6) (1a)

parameters	values
empirical formula	$C_{33}H_{29}F_6FeN_5O_3P$
FW	744.43
crystal system	triclinic
space group	$P\bar{1}$
a (Å)	10.357(2)
b (Å)	11.440(3)
c (Å)	14.297(4)
α (deg)	99.748(11)
β (deg)	95.099(11)
γ (deg)	101.668(10)
V (Å^3)	1621.7(7)
Z	2
T (K)	296 (2)
ρ_{calcd} (g cm^{-3})	1.525
λ (Å) (Mo K_α)	0.71073
μ (mm^{-1})	0.592
data/restraints/parameters	5659/0/442
F(000)	762
goodness of fit	1.084
R (F_o)^a, $I > 2\sigma(I)$/wR (F_o)^b	0.0592/0.1588
R (all data)/wR (all data)	0.0866/0.1735
largest diff peak and hole (e Å^{-3})	1.770, −0.334

$^aR = \Sigma||F_o| - |F_c||/\Sigma|F_o|$. $^bwR = \{\Sigma[w(F_o^2 - F_c^2)^2]/\Sigma[w(F_o)^2]\}^{1/2}$. $w = [(\sigma F_o)^2 + (AP)^2 + BP]^{-1}$, where $P = (F_o^2 + 2F_c^2)/3$.

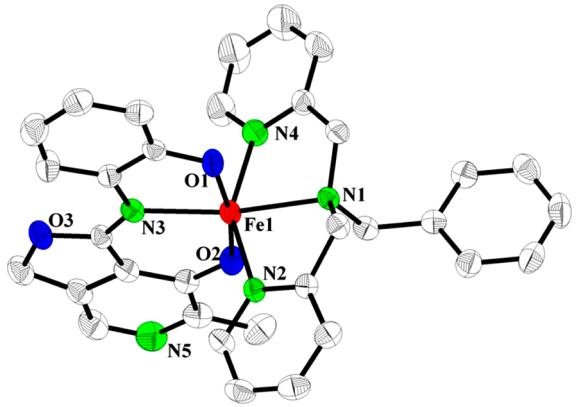

Figure 2. ORTEP diagram of the cationic complex in [Fe(phbpa)-(L^1)](PF_6) (1a) showing the thermal ellipsoids at 50% probability and the labeling of the metal and heteroatoms. The hydrogen atoms are omitted for clarity. Color codes: metal, red; nitrogen, green; oxygen, blue; carbon, white.

structure showed a distorted octahedral FeN_4O_2 core with the tridentate ligands coordinating to the metal in the facial mode. The pyridoxal Schiff base coordinated through two phenolic oxygen atoms and a nitrogen atom. The Fe(1)−O(1) and Fe(1)−O(2) bond lengths were 1.926(3) and 1.920(3) Å, respectively. The Fe−N distances varied from 2.128(3) to 2.222(3) Å. The Fe(1)−N(1) distance is longer compared to the other Fe−N bond lengths. The hydroxyl group of the pyridoxal moiety was seen to undergo cyclization forming a five-member ring (Figure S13, Supporting Information). The pyridoxal Schiff base binding to other metal ions does not show a similar cyclization process.[28,47] Thus, it appears that Fe^{3+} being a strong Lewis acid promotes such *in situ* cyclization of the ligand. This is corroborated by similar observation as mentioned above where Lewis acids or protic acids promote such novel cyclization reactions.[42−44]

Theoretical Studies. DFT calculations were carried out using B3LYP level theory with LanL2DZ basis set with Gaussian 09 programs to get further insights on the excited state properties of complexes **1**−**3**. The initial coordinates were obtained from the crystal structure of **1a** and were used for optimization (Table S1, Supporting Information). TDDFT calculations were carried out on the geometrically optimized structures of **1**−**3** to assign the transitions obtained in the UV−visible spectra. The dipole allowed transitions along with the oscillator strengths for all three complexes are listed in Table S2 (see Supporting Information). A strong LMCT was observed theoretically near 590 nm which corresponds to the transition from the phenolate π^* orbitals to the dπ orbitals of the metal in **1**. Additionally, in complexes **2** and **3**, the anthracenyl and pyrenyl groups also contribute strongly to this LMCT band. This could explain the excellent photocytotoxicity of **2** and **3** but not **1**. The other transitions above 400 nm also correspond mainly to LMCT transitions involving the orbitals of phenolate and the iron. Transitions below 400 nm correspond to intraligand charge transfer (ILCT) transitions involving both the dipicolylamine and the Schiff base ligands. In fact, the HOMOs of complexes **2** and **3** primarily involved the electron-rich anthracenyl or pyrenyl groups but not so in the case of the phenyl analogue in complex **1**. The LUMO was based on the dipicolylamine moiety in complexes **2** and **3** (Figure 3).

Solubility and Stability. Complexes **1**−**3** were soluble in water, methanol, ethanol, dichloromethane, dimethylformamide, and dimethyl sulfoxide. They were insoluble in hydrocarbon solvents such as hexane, xylene, or toluene. Complexes **4** and **5** were sparingly soluble in water. To examine the biological activity of the complexes, it is a prerequisite that

Table 3. Selected Bond Lengths and Bond Angles of [Fe(phbpa)(L^1)](PF_6) (1a)

bond	bond length (Å)	bond	bond angle (deg)
Fe(1)−O(1)	1.927(3)	O(1)−Fe(1)−N(4)	90.37(13)
Fe(1)−O(2)	1.922(3)	O(2)−Fe(1)−N(1)	102.63(11)
Fe(1)−N(1)	2.222(3)	O(2)−Fe(1)−N(2)	90.78(11)
Fe(1)−N(2)	2.128(3)	O(2)−Fe(1)−N(3)	91.24(11)
Fe(1)−N(3)	2.144(3)	O(2)−Fe(1)−N(4)	90.63(13)
Fe(1)−N(4)	2.137(3)	N(1)−Fe(1)−N(2)	76.11(11)
bond	bond angle (deg)	N(1)−Fe(1)−N(3)	166.03(11)
O(1)−Fe(1)−O(2)	169.55(11)	N(1)−Fe(1)−N(4)	74.97(11)
O(1)−Fe(1)−N(1)	87.68(11)	N(2)−Fe(1)−N(3)	105.74(11)
O(1)−Fe(1)−N(2)	93.44(11)	N(2)−Fe(1)−N(4)	150.63(13)
O(1)−Fe(1)−N(3)	78.41(11)	N(3)−Fe(1)−N(4)	103.55(12)

DOI: 10.1021/ic5027625
Inorg. Chem. XXXX, XXX, XXX−XXX

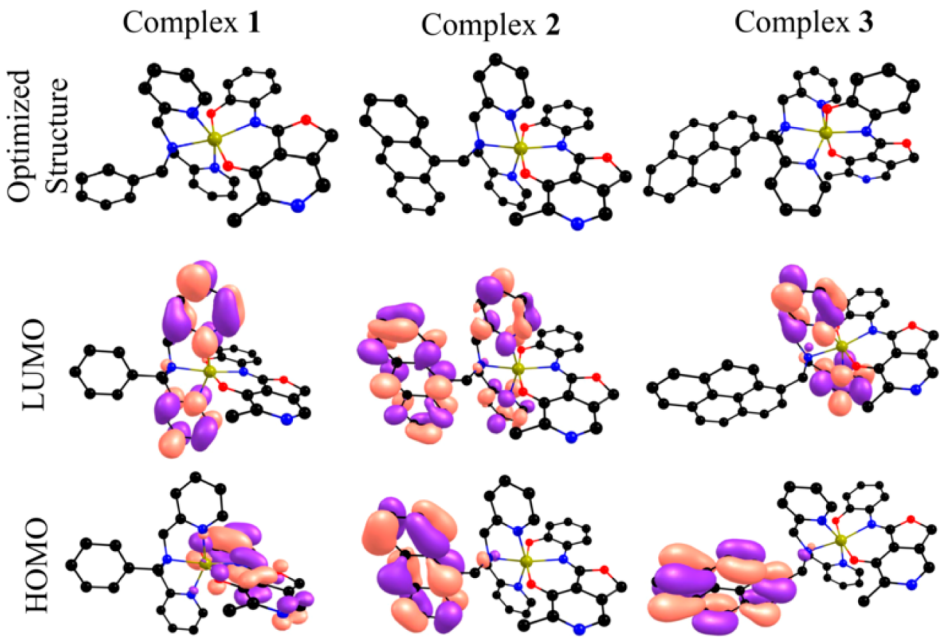

Figure 3. Geometrically optimized structures of complexes **1**−**3** obtained from DFT calculations using B3LYP level and LanL2DZ basis set and the frontier molecular orbitals for the same obtained from TDDFT calculations.

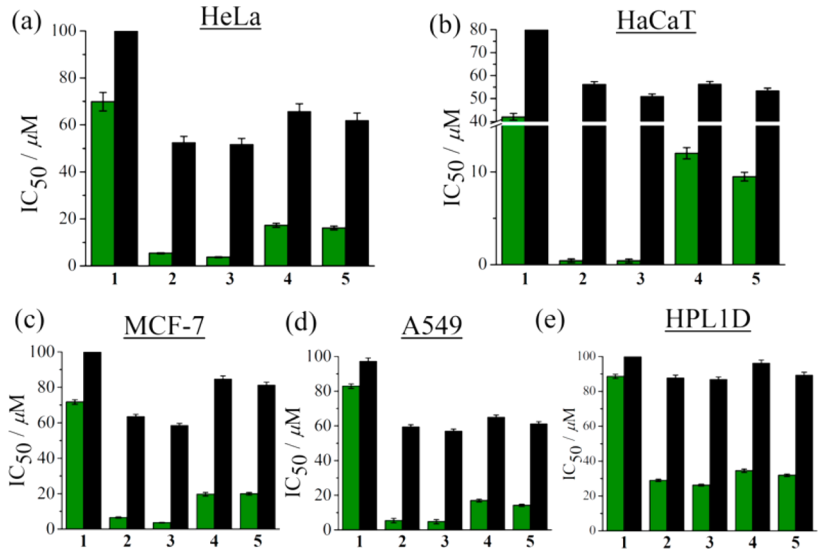

Figure 4. Bar diagrams showing the cytotoxicity of the complexes **1**−**5** in different cells lines upon irradiation with visible light (400−700 nm, 10 J cm^{-2}, green bars) and in dark (black bars): HeLa (a), HaCaT (b), MCF-7 (c), A549 (d), and HPL1D (e).

they are stable under physiological conditions. The stability of the complexes was thus monitored in DMSO−DPBS (1:1 v/v) for 24 h using UV−visible spectral scans. There was no significant shift of the absorption bands or appearance of any new peaks (Figure S14, Supporting Information). The intensity of the bands also remained essentially similar, which rules out the possibility of any degradation of the complexes in physiological conditions or leaching of the metal ion in the solution phase.

Cytotoxicity. The cytotoxicity of complexes **1**−**5** and the ligands was examined in different cell lines, namely, HeLa (human cervical cancer), MCF-7 (human breast cancer), HaCaT (human keratinocytes), A549 (lung adenocarcinoma), and HPL1D (nontransformed human epithelial lung cells) (Figure 4, Figures S15−S20, Supporting Information). The IC_{50} values of the complexes, ligands along with few related compounds are listed in Table 4.[27,48−50] HaCaT cells were chosen as a model for superficial cells, and HPL1D served as the control normal cell line. The cells were incubated with different concentrations of the complexes or the ligands for 4 h in dark. Complex **1** did not show any significant photocytotoxicity when irradiated with visible light (400−700 nm). However, pyridoxal appended complexes **2** and **3** were remarkably active with IC_{50} values ranging from 0.4 to 5 μM in different cells under identical experimental conditions in HeLa, HaCaT, MCF-7, and A549 cells. The corresponding control complexes **4** and **5** were rather less cytotoxic with IC_{50} values >20 μM. The complexes did not show any pronounced dark toxicity with IC_{50} values >50 μM. Again, complexes **2** and **3** were 6-fold less cytotoxic in normal lung cell line HPL1D

DOI: 10.1021/ic5027625
Inorg. Chem. XXXX, XXX, XXX−XXX

Table 4. IC_{50} Values (μM) of Complexes 1−5[a] and Related Compounds in Various Cell Lines

cell lines	HeLa		HaCaT		MCF-7		A549		HPL1D	
complex	L[b]	D[c]	L[b]	D[c]	L[b]	D[c]	L[b]	D[c]	L[b]	D[c]
1	70.4 ± 1.2	>100	41.8 ± 1.1	93.0 ± 1.0	71.8 ± 1.3	>100	82.9 ± 1.3	97.2 ± 1.9	88.6 ± 1.2	>100
2	5.5 ± 1.3	56.0 ± 1.4	0.41 ± 0.20	54.2 ± 1.1	6.6 ± 0.3	63.5 ± 1.3	5.4 ± 1.3	59.5 ± 1.2	29.0 ± 0.7	87.7 ± 1.6
3	3.3 ± 1.1	53.5 ± 1.6	0.41 ± 0.10	53.4 ± 2.1	3.7 ± 0.2	58.5 ± 1.2	4.8 ± 1.2	57.0 ± 1.2	26.3 ± 0.6	86.9 ± 1.4
4	18.8 ± 1.3	86.8 ± 2.5	8.4 ± 2.2	52.6 ± 1.7	19.7 ± 1.0	84.7 ± 1.7	17.1 ± 0.9	65.9 ± 1.3	34.5 ± 1.0	96.2 ± 1.7
5	16.1 ± 1.2	62.9 ± 2.7	7.2 ± 1.4	57.1 ± 2.0	20.0 ± 0.8	81.9 ± 1.6	14.2 ± 0.7	61.2 ± 1.2	31.9 ± 0.8	89.3 ± 1.6
$[Fe(anbpa)(cat)(NO_3)]$[d]	6.2 ± 0.1	>100	14.1 ± 0.1	>100	11.3 ± 0.1	>100				
$[Fe(bpyag)(pyap)](NO_3)$[e]	8.2 ± 0.6	87.4 ± 1.2	14.5 ± 1.3	>100						
[Fe(pybpa)(BHA)Cl][f]	14.6 ± 0.7	77.0 ± 1.1								

[a]The IC_{50} values of the ligands in HeLa cells are anbpa, 27.4 ± 1.5 μM in light and 49.0 ± 2.2 μM in dark; pybpa, 35.3 ± 1.7 μM in light and 44.6 ± 1.3 μM in dark; H_2L^1, >100 μM in light and dark; and H_2L^2, >100 μM in light and dark. [b]IC_{50} values in visible light (400−700 nm, 10 J cm^{-2}, L). [c]IC_{50} values in dark (D). [d]Reference 27. [e]Reference 48. [f]Reference 49. The IC_{50} value of an iron(II) complex $[Fe(Hqpy)(MeCN)_2](ClO_4)_2$ in dark with incubation time of 48 h is 4.0 μM [Hqpy 2,2′:6′,2″:6″,2‴:6‴,2⁗-quinquepyridine (ref 50)].

with the IC_{50} value in light being >30 μM (Table 4). A comparison of the IC_{50} values in cancerous and normal cell lines of the same origin (A549 and HPL1D) shows the distinct selectivity with which the molecules affect the cancer cells. Thus, the selective photocytotoxicity of the complexes having pyridoxal derivative toward cancer cells over normal cells is a manifestation of the better uptake properties of the VB6 group, which adds a new dimension to the PDT agents under study. Again, the anthracene or pyrene conjugated dipicolylamine ligands showed moderate cytotoxicity and photocytotoxicity under identical experimental conditions in HeLa cells (Table 4, Figure S20, Supporting Information). Similarly, the Schiff base ligands were nontoxic in HeLa cells irrespective of the presence or absence of light (Figure S20, Supporting Information). The broad band 400−700 nm light source (Luzchem Photoreactor) was used due to the presence of the LMCT band of the complexes in the green light region.

Cellular Incorporation Studies. The percent cell positivity of the complexes **2**−**5** in HeLa and HaCaT cells were thus monitored using FACS analysis. After the cells were incubated for 4 h with the complexes in the dark, complexes **2** and **3** displayed nearly 90% of the cells showing positive signal for complex uptake, while only about 30% of the cells showed a positive response upon treatment with **4** and **5** (Figure 5). Our hypothesis is that the internalization of the complexes of pyridoxal derivative (**2** and **3**) is more facile as compared to complexes **4** and **5** which lack such a group.

In another experiment, the cells were incubated with pyridoxal hydrochloride for 4 h prior to addition of the complexes, and the cellular internalization was monitored. The FACS analysis showed significant lowering of the fluorescence signal (∼15%) for complexes **2** and **3**, which corresponds to fewer number of cells taking up the complexes. Complexes **4** and **5** also showed a reduced fluorescence signal albeit much less. This effect was again more pronounced in HeLa cells compared to the HaCaT cells. Hence it can be inferred that the presence of a VB6-like group in complexes **2** and **3** somehow enhances the cellular uptake properties especially in the cancer cells, which results in better cytotoxicity after light irradiation. This is of paramount importance where the VB6 tagged complexes are preferentially internalized in cancer cells which induce a higher degree of selectivity to the PDT agent as compared to the conventional PDT drugs where the selectivity is induced only with light irradiation.

Dose-Dependent Cellular Uptake. A dose-dependent cellular uptake of **3** and **5** was monitored in HeLa cells by varying the concentration of VB6 (pyridoxal hydrochloride). HeLa cells were treated with various concentrations of pyridoxal hydrochloride (2, 1.5, 1.0, 0.5, 0.25, and 0.1 mM) for 4 h in the dark followed by addition of either of the complexes. It was observed that with the lowering of the concentration of VB6, there was a stark increase in the percent positivity of cells to which complex **3** was added. However, there was no such marked dose-dependent increase in the mean fluorescence of the cells that were treated with complex **5**. This observation can be related with the presence of the pendant group resembling pyridoxal, which probably assists in cellular uptake of the complexes (Figure S21, Supporting Information).

Cell Cycle Analysis. The effect of the photocytotoxic complexes on the progression of the cell cycle was studied by FACS analysis in HeLa and HaCaT cells treated with the complexes **1**−**5** in light of 400−700 nm or in the dark. Before analysis, the cells were treated with PI that stains the DNA

DOI: 10.1021/ic5027625
Inorg. Chem. XXXX, XXX, XXX−XXX

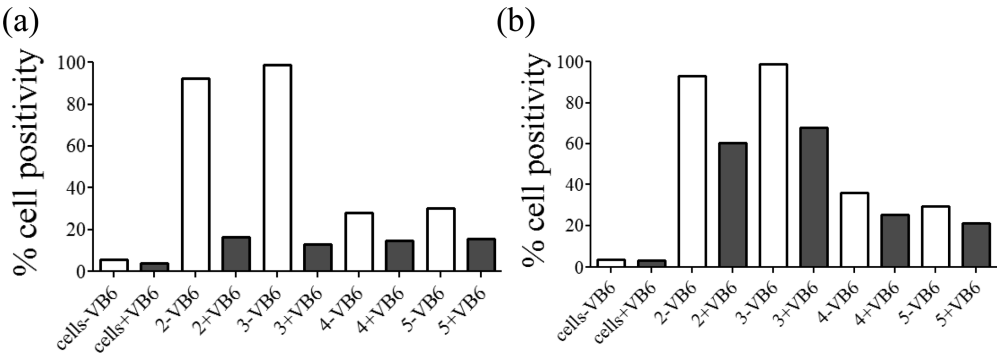

Figure 5. Percent cell positivity upon treatment with the complexes **2**–**5** in HeLa (a) and HaCaT (b) cells with (black bars) or without VB6 derivative (white bars) indicating the internalization of the complexes inside the cells.

quantitatively. Hence, the fluorescence intensity of the stained cells correlates with the amount of DNA. The sub G1 population of the cells corresponds to those whose membrane has been compromised and have undergone cell death. Complex **1** did not alter the cell cycle progression in light or in the dark in either HeLa or HaCaT cells. It was seen that both **2** and **3** induced significant sub G1 population compared to **4** and **5** in HaCaT cells upon exposure to light. The percentage of sub G1 population induced by **2** and **3** in HeLa cells was nearly 30%. Treatment of cells with complexes **4** or **5** followed by irradiation resulted in the arrest of the G2/M phase (Figure 7, Figures S21 and S22, Supporting Information). The complexes of pyridoxal base thus have enhanced cellular uptake as evidenced from the cell cycle profiling analysis.

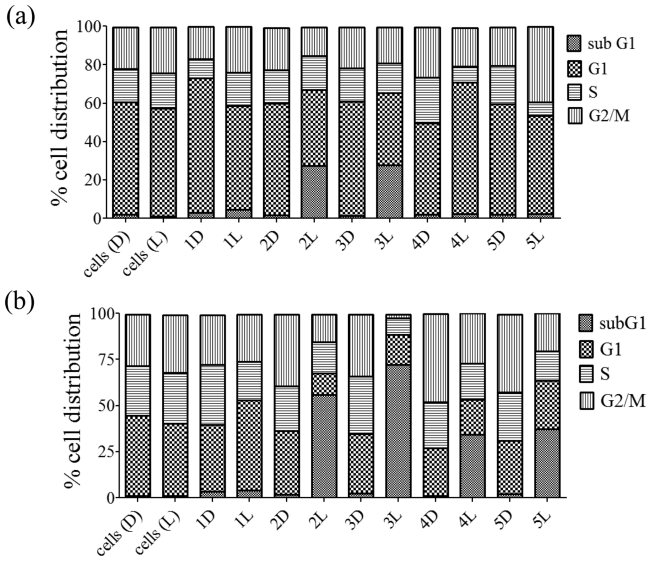

Figure 6. Cell cycle progression in cells alone or after treatment with the complexes **2**–**5** in the dark (D) or upon irradiation with visible light (400–700 nm, 10 J cm^{-2}, L) in HeLa (a) and HaCaT (b) cells showing the percentage of cells in different phases of the cell cycle.

Annexin-V-FITC/PI Assay. The cells in the early stages of apoptosis undergo morphological changes including the translocation of phosphatidylserine to the external portion of the lipid bilayer. To estimate the number of cells undergoing apoptosis, we performed the Annexin-V-FITC/PI assay using complexes **2**–**5** in HeLa cells. Cells were incubated with the complexes for 4 h in dark followed by light irradiation (400–700 nm). Complexes **2** and **3** induced features of early

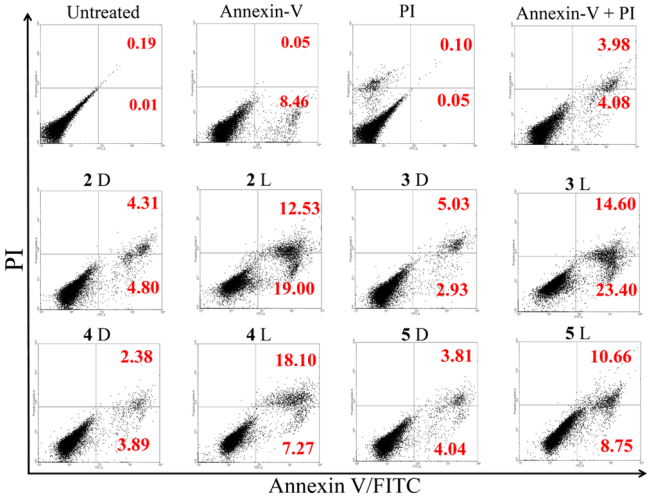

Figure 7. Annexin-V-FITC/PI assay showing the percent population of early apoptotic cells stained by annexin-V-FITC alone (lower right quadrant), dead cells stained by propidium iodide alone (upper left quadrant), or late apoptotic cells stained by both annexin-V-FITC and PI (upper right quadrant) in HeLa cells alone or treated with complexes **2**–**5** in the dark (D) or after exposure to visible light (400–700 nm, L).

apoptosis in ~25% of the cells when irradiated with visible light compared to ~8% for complexes **4** and **5** under identical experimental conditions. A prominent fraction of cells showed features of late apoptosis for all four complexes (Figure 8).

DCFDA Assay. 2′,7′-Dichlorofluorescein diacetate (DCFDA) assay was done to detect generation of any cellular ROS. The percentage of cell population generating ROS can be determined by flow cytometry analysis. To ascertain the formation of ROS inside the cells, HeLa or HaCaT cells were incubated with **2** and **3** for 4 h in the dark, and then one of the plates was exposed to light irradiation (400–700 nm) for 1 h. The cells treated with these complexes and light showed a significant shift in the cell population showing fluorescence as compared to those kept in the dark (Figure 9, Figure S23, Supporting Information). This indicates the formation of ROS which is believed to be responsible for the cell death only upon photoirradiation but not in the dark. Hydrogen peroxide was used as a positive control for the experiment. When cytotoxicity assay was performed in the presence of *N*-acetyl cysteine (NAC) as a ROS scavenger, there was a significant increase in the IC_{50} values for complexes **2**–**5** in HeLa cells in identical

DOI: 10.1021/ic5027625
Inorg. Chem. XXXX, XXX, XXX–XXX

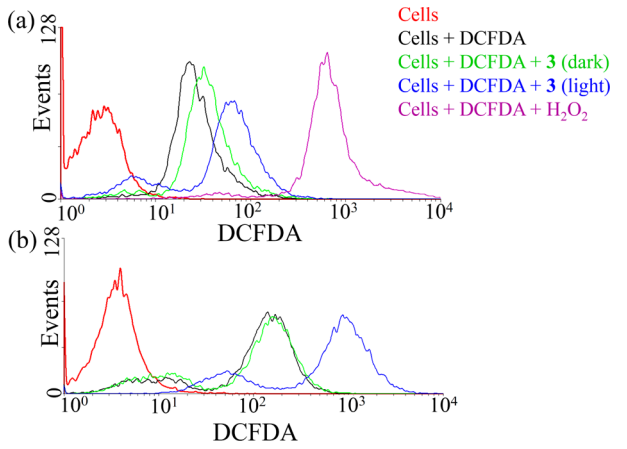

Figure 8. Increase in fluorescence of DCF in HeLa (above) or HaCaT (below) cells upon treatment with complex **3** on light irradiation (400–700 nm, 10 J cm^{-2}) or in dark with H_2O_2 used as a positive control.

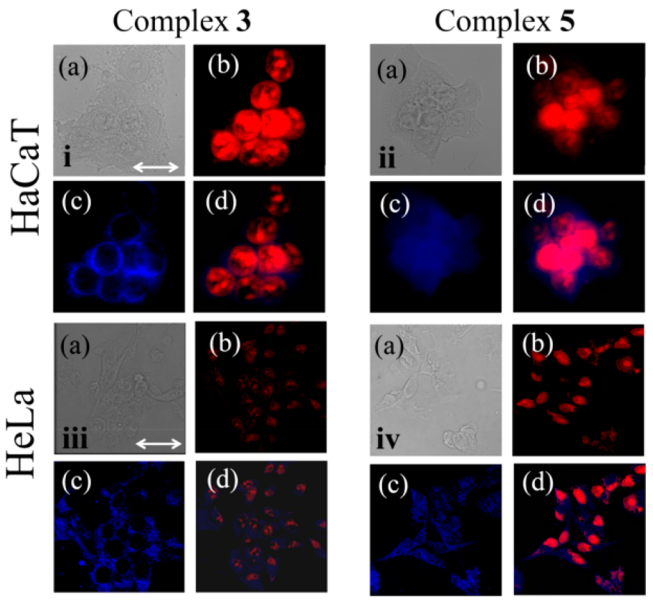

Figure 9. Confocal microscopy images of HaCaT (panels: (i) and (ii)) and HeLa cells (panels: (iii) and (iv)) treated with propidium iodide (PI) as the nucleus marker and complex **3** or **5** as labeled. Panels (a) show the bright field images of the cells, panels (b) show the fluorescence of propidium iodide, panels (c) show the fluorescence of either complex **3** or **5**, and panels (d) show the merged images of the PI and complex **3** or **5**. The scale bar corresponds to 20 μm.

experimental conditions, which reaffirms the role of ROS in cell death (Figure S24, Supporting Information).

Cellular Localization. The localization of the complexes **2**–**5** inside the HeLa and HaCaT cells was monitored by confocal microscopy using nuclear staining dye propidium iodide (PI). Co-localization studies indicated that complexes **2** and **3** primarily accumulate in certain portions of the cytoplasm of the cells with no significant nuclear uptake. Though complexes **4** and **5** showed a diffused distribution throughout the cell, complexes **2** and **3** of VB6 derivative showed very distinct accumulation in the periphery of the nucleus in both cell lines as can be seen in the panels i(c) and iii(c) of Figure 10 (Figure S25, Supporting Information).

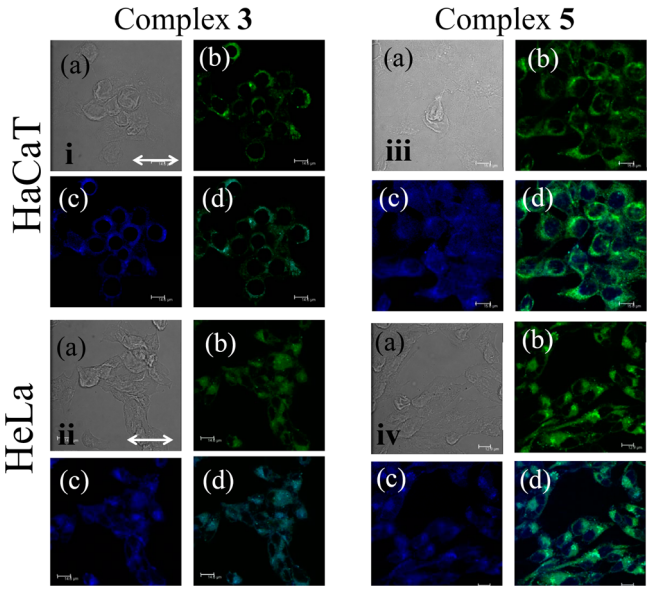

Figure 10. Confocal microscopy images of HaCaT (panels (i) and (ii)) and HeLa cells (panels (iii) and (iv)) treated with ER tracker green as the endoplasmic reticulum (ER) marker and complexes **3** or **5** as labeled. Panels labeled (a) show the bright field images of the cells, panels labeled (b) show the fluorescence of ER tracker green, panels labeled (c) show the fluorescence of either complex **3** or **5**, and panels labeled (d) show the merged images of the ER tracker green and complex **3** or **5**. The scale bars are 14.6 μm.

With the knowledge that the ER forms channel-like structures at the nuclear periphery, we performed colocalization studies with ER tracker green and complexes **2** and **3**. The merged images in Figure 10 show the exact overlap of the fluorescence of ER tracker and the complexes. Similar experiments with complexes **4** and **5** show only a diffused blue fluorescence throughout the cell (Figure S26, Supporting Information). Thus, we infer that the complexes of VB6 derivative localize in the ER of the cells and upon irradiation generate ROS which results in ER stress. Followed by such a cascade of events, the cells eventually undergo apoptotic death. Again, complexes **4** and **5** do not show such specific targeting and display a general accumulation in the cytoplasm and the nucleus. So the pyridoxal derivative is implicated in the preferential localization of the complexes in the ER. This observation is both interesting and important since detouring chemotherapeutic molecules from their conventional target, i.e., the nucleus, to other organelles is likely to have positive effects on their anticancer properties.

CONCLUSIONS

Ternary iron(III) Schiff base complexes of a VB6 derivative show specific accumulation into the cancer cells compared to the control complexes lacking the pyridoxal moiety and exhibit remarkable photocytotoxicity when irradiated with visible light (400–700 nm) while remaining innocuous in the dark. The complexes are five to six times less cytotoxic in normal lung cells. They induce apoptotic cell death in HeLa or HaCaT cells with the generation of ROS. An interesting observation is that the VB6 derivative Schiff base complexes accumulate predominantly in the ER of the cells as opposed to the control complexes of similar make which resided in both the cytoplasm and nucleus of the cells. Such molecules which can target organelles other than the nucleus can dodge the NER

DOI: 10.1021/ic5027625
Inorg. Chem. XXXX, XXX, XXX–XXX

mechanism, which often leads to intrinsic resistance of cells to the chemotherapeutic agents. The apoptotic cell death through ERSR thus offers a new strategic way in PDT, and the development of such molecules can confer a higher degree of selectivity to novel PDT agents which can target cancer cells and cause cell death.

■ ASSOCIATED CONTENT

Supporting Information

All the details of the experimental procedures, reaction schemes (Schemes S1, S2), NMR (Figures S1, S3), ESI-MS (Figures S2, S4−S9), IR spectra (Figure S10), cyclic voltammograms (Figure S11), crystal structure (Figures S12 and S13), UV−visible data for stability of the complexes (Figure S14), MTT assay (Figures S15−S20, S25), dose-dependent cellular incorporation (Figure S21), FACS analysis (Figures S22, S23), DCFDA assay (Figure S24), confocal images (Figures S26, S27), Tables S1 and S2 giving Cartesian coordinates and electronic transitions in the complexes. This material is available free of charge via the Internet at http://pubs.acs.org.

■ AUTHOR INFORMATION

Corresponding Authors

*(P.K.) E-mail: paturu@mrdg.iisc.ernet.in. Tel.: +91-80-22932688. Fax: +91-80-23600999.

*(A.R.C.) E-mail: arc@ipc.iisc.ernet.in. Tel.: +91-80-22932533. Fax: +91-80-23600683.

Notes

The authors declare no competing financial interest.

■ ACKNOWLEDGMENTS

We thank the Department of Science and Technology (DST), Government of India, and the Council of Scientific and Industrial Research (CSIR), New Delhi, for financial support (SR/S5/MBD-02/2007; CSIR/01(2559)/12/EMR-II/2012). A.R.C. thanks the DST for J. C. Bose national fellowship and the Alexander von Humboldt Foundation, Germany, for donation of an electrochemical system. We are thankful to Mr. Vashista K. and Ms. A. Kavya for the FACS analysis and Dr. Santosh Poddar for the confocal microscopy images.

■ DEDICATION

Dedicated to Professor Animesh Chakravorty on the occasion of his 80th birthday.

■ REFERENCES

(1) Wenner, C. E. *J. Cell Physiol.* **2012**, *227*, 450−456.
(2) Fulda, S.; Galluzzi, L.; Kroemer, G. *Nat. Rev. Drug Discovery* **2010**, *9*, 447−467.
(3) Armstrong, J. S. *Br. J. Pharmacol.* **2006**, *147*, 239−248.
(4) Damia, G.; Imperatori, L.; Stefanini, M.; D'Incalci, M. *Int. J. Cancer* **1996**, *66*, 779−783.
(5) Marrachea, S.; Tundup, S.; Harn, D. A.; Dhar, S. *ACS Nano* **2013**, *7*, 7392−7402.
(6) Basu, A.; Krishnamurthy, S. *J. Nucleic Acid* **2010**, No. 201367.
(7) Rosell, R.; Taron, M.; Barnadas, A.; Scagliotti, G.; Sarries, C.; Roig, B. *Cancer Control* **2003**, *10*, 297−305.
(8) Pierozz, V.; Joshi, T.; Leonidova, A.; Mari, C.; Schur, J.; Ott, I.; Spiccia, L.; Ferrari, S.; Gasser, G. *J. Am. Chem. Soc.* **2012**, *134*, 20376−20387.
(9) Millard, M.; Gallagher, J. D.; Olenyuk, B. Z.; Neamati, N. *J. Med. Chem.* **2013**, *56*, 9170−9179.
(10) Marrache, S.; Pathak, R. K.; Dhar, S. *Proc. Natl. Acad. Sci. U.S.A.* **2014**, *111*, 10444−10449.
(11) Marrache, S.; Dhar, S. *Proc. Natl. Acad. Sc. USA* **2012**, *109*, 16288−16293.
(12) Celli, J. P.; Spring, B. Q.; Rizvi, I.; Evans, C. L.; Samkoe, K. S.; Verma, S.; Pogue, B. W.; Hasan, T. *Chem. Rev.* **2010**, *110*, 2795−2838.
(13) Kinzler, I.; Haseroth, E.; Hauser, C.; Rűck, A. *Photochem. Photobiol. Sci.* **2007**, *6*, 1332−1340.
(14) Atlante, A.; Passarella, S.; Quagliariello, E. *Photochem. Photobiol. B* **1989**, *4*, 35−46.
(15) Li, L. B.; Luo, R. C. *Lasers Med. Sci.* **2009**, *24*, 597−603.
(16) Ormond, A. B.; Freeman, H. S. *Materials* **2013**, *6*, 817−840.
(17) Chakrabarti, M.; Banik, N. L.; Ray, S. K. *PLoS One* **2013**, *8*, e55652.
(18) Romero-Canelón, I.; Sadler, P. J. *Inorg. Chem.* **2013**, *52*, 12276−12291.
(19) Verfaillie, T.; Garg, A. D.; Agostinis, P. *Cancer Lett.* **2010**, *332*, 249−264.
(20) Tabas, I.; Ron, D. *Nat. Cell Biol.* **2011**, *13*, 184−190.
(21) Schönthal, A. H. *Biochem. Pharmacol.* **2013**, *85*, 653−666.
(22) Schroder, M. *Cell. Mol. Life Sci.* **2008**, *65*, 862−894.
(23) Garg, A.; Martin, S.; Golab, J.; Agostinis, P. *Cell Death Differ.* **2014**, *21*, 26−38.
(24) Bonnett, R. *Chemical Aspects of Photodynamic Therapy*; Gordon & Breach: London, U.K., 2000.
(25) Ethirajan, M.; Chen, Y.; Joshi, P.; Pandey, R. K. *Chem. Soc. Rev.* **2011**, *40*, 340−362.
(26) Smith, N. A.; Sadler, P. J. *Philos. Trans. R. Soc. A* **2013**, *371*, 20120519.
(27) Basu, U.; Khan, I.; Hussain, A.; Kondaiah, P.; Chakravarty, A. R. *Angew. Chem., Int. Ed.* **2012**, *51*, 2658−2661.
(28) Banerjee, S.; Dixit, A.; Shridharan, R. N.; Karande, A. A.; Chakravarty, A. R. *Chem. Commun.* **2014**, *50*, 5590−5592.
(29) Hellmann, H.; Mooney, S. *Molecules* **2010**, *15*, 442−459.
(30) Mooney, S.; Leuendorf, J. E.; Hendrickson, C.; Hellmann, H. *Molecules* **2009**, *14*, 329−351.
(31) Zhang, P.; Suidasari, S.; Hasegawa, T.; Yanaka, N.; Kato, N. *Oncol. Rep.* **2014**, *31*, 2371−2376.
(32) Pandey, S.; Garg, P.; Lim, K. T.; Kim, J.; Choung, Y. H.; Choi, Y. J.; Choung, P. H.; Cho, C. S.; Chung, J. H. *Biomaterials* **2013**, *34*, 3716−3728.
(33) Pandey, S.; Garg, P.; Lee, S.; Choung, H. W.; Choung, Y. H.; Choung, P. H.; Chung, J. H. *Biomaterials* **2014**, *35*, 9332−9342.
(34) McCormick, D. B.Vitamin B6 transport and metabolism: Clues for delivery of bioactive compounds. In *Biochemistry of Vitamin B6, Advances in Life Sciences*, Marino, G., Sannia, G., Bossa, F., Eds.; Birkhäuser Verlag: Basel, 1994; pp 311−317.
(35) Spector, R.; Johanson, C. E. *J. Neurochem.* **2007**, *103*, 425−438.
(36) Said, H. M.; Ortiz, A.; Ma, T. Y. *Am. J. Physiol. Cell Physiol.* **2003**, *285*, C1219−C1225.
(37) Perrin, D. D.; Armarego, W. L. F.; Perrin, D. R. *Purification of Laboratory Chemicals*; Pergamon Press: Oxford, 1980.
(38) Basu, U.; Pant, I.; Khan, I.; Hussain, A.; Kondaiah, P.; Chakravarty, A. R. *Chem.—Asian J.* **2014**, *9*, 2494−2504.
(39) Frisch, M. J.; Trucks, G. W.; Schlegel, H. B.; Scuseria, G. E.; Robb, M. A.; Cheeseman, J. R.; Montgomery, J. A.; Vreven, T.; Kudin, K. N.; Burant, J. C.; Millam, J. M.; Iyengar, S. S.; Tomasi, J.; Barone, V.; Mennucci, B.; Cossi, M.; Scalmani, G.; Rega, N.; Petersson, G. A.; Nakatsuji, H.; Hada, M.; Ehara, M.; Toyota, K.; Fukuda, R.; Hasegawa, J.; Ishida, H.; Nakajima, T.; Honda, Y.; Kitao, O.; Nakai, H.; Klene, M.; Li, X.; Knox, J. E.; Hratchian, H. P.; Cross, J. B.; Adamo, C.; Jaramillo, J.; Gomperts, R.; Stratmann, R. E.; Yazyev, O.; Austin, A. J.; Cammi, R.; Pomelli, C.; Ochterski, J.; Ayala, P. Y.; Morokuma, K.; Voth, G. A.; Salvador, P.; Dannenberg, J. J.; Zakrzewski, V. G.; Dapprich, S.; Daniels, A. D.; Strain, M. C.; Farkas, O.; Malick, D. K.; Rabuck, A. D.; Raghavachari, K.; Foresman, J. B.; Ortiz, J. V.; Cui, Q.; Baboul, A. G.; Clifford, S.; Cioslowski, J.; Stefanov, B. B.; Liu, G.; Liashenko, A.; Piskorz, P.; Komaromi, I.; Martin, R. L.; Fox, D. J.; Keith, T. ; Al-Laham, M. A.; Peng, C. Y.; Nanayakkara, A.; Challacombe, M.; Gill, P. M. W.; Johnson, B.; Chen, W.; Wong, M. W.; Gonzalez, C.; Pople, J. A. *Gaussian 03*, Revision B.4; Gaussian Inc.: Pittsburgh, PA, 2003.

DOI: 10.1021/ic5027625
Inorg. Chem. XXXX, XXX, XXX−XXX

(40) Becke, A. D. *J. Chem. Phys.* **1993**, *98*, 5648−5652.
(41) Tomasi, J.; Persico, M. *Chem. Rev.* **1994**, *94*, 2027−2094.
(42) Kumar, A.; Kumar, D. *Asian J. Chem.* **2008**, *20*, 1588−1592.
(43) Roy, M.; Patra, A. K.; Mukherjee, A.; Nethaji, M.; Chakravarty, A. R. *Indian J. Chem. A* **2007**, *46*, 227−237.
(44) Kierska, D.; Maśliński, Cz. *Biochem. Pharmacol.* **1971**, *20*, 1951−1959.
(45) Velusamy, M.; Palaniandavar, M. *Inorg. Chem.* **2003**, *42*, 8283−8293.
(46) Palaniandavar, M.; Velusamy, M.; Mayilmurugan, R. *J. Chem. Sci.* **2006**, *118*, 601−610.
(47) Ozawa, T.; Jitsukawa, K.; Masuda, H.; Einaga, H. *Polyhedron* **1995**, *14*, 1999−2007.
(48) Basu, U.; Khan, I.; Hussain, A.; Gole, B.; Kondaiah, P.; Chakravarty, A. R. *Inorg. Chem.* **2014**, *53*, 2152−2162.
(49) Garai, A.; Basu, U.; Khan, I.; Pant, I.; Hussain, A.; Kondaiah, P.; Chakravarty, A. R. *Polyhedron* **2014**, *73*, 124−132.
(50) Wong, E. L. M.; Fang, G. S.; Che, C. M.; Zhu, N. *Chem. Commun.* **2005**, 4578−4580.

DOI: 10.1021/ic5027625
Inorg. Chem. XXXX, XXX, XXX−XXX